JOURNAL OF GEOPHYSICAL RESEARCH, VOL. 115, D00K12, doi:10.1029/2009JD013263, 2010

Dust aerosol optical properties retrieval and radiative forcing over northwestern China during the 2008 China-U.S. joint field experiment

J. M. Ge,[1,2] J. Su,[1,2] T. P. Ackerman,[2] Q. Fu,[1,2] J. P. Huang,[1] and J. S. Shi[1]

Received 24 September 2009; revised 29 January 2010; accepted 18 February 2010; published 15 July 2010.

[1] The Atmosphere Radiation Measurements Program's Ancillary Facility (AAF/SMART-COMMIT) was deployed to Zhangye (39.082°N, 100.276°E), which is located in a semidesert area of northwest China, during the period of late April to mid June in 2008. We selected 11 cases to retrieve dust aerosol optical depth (AOD), Angstrom exponent, size distribution, single-scattering albedo (SSA) and asymmetry parameter (ASY) from multifilter rotating shadowband radiometer (MFRSR) measurements. These cases are dominated by large particles with Angstrom exponent values ranging from 0.34 to 0.93. The values of AOD at 0.67 μm range from 0.07 to 0.25. The mean SSA value increases with wavelength from 0.76 ± 0.02 at 0.415 μm to 0.86 ± 0.01 at 0.870 μm, while the mean ASY value decreases from 0.74 ± 0.04 to 0.70 ± 0.02. Before estimating dust aerosol direct radiative forcing, a radiative closure experiment was performed to verify that the retrieved aerosol optical properties and other input parameters to the radiative transfer model appropriately represent atmospheric conditions. The daytime-averaged differences between model simulations and ground observations are −8.5, −2.9, and −2.1 W m^{-2} for the total, diffuse, and direct normal fluxes, respectively. The mean difference in the instantaneous reflected solar fluxes at the top of atmosphere (TOA) between the model and CERES observations is 8.0 W m^{-2}. The solar aerosol direct radiative forcing (ARF), averaged over a 24 h period, at the surface is −22.4 ± 8.9 W m^{-2}, while the TOA ARF is small and has an average value of only 0.52 ± 1.69 W m^{-2}. The daily averaged surface aerosol radiative forcing efficiency at 0.5 μm is −95.1 ± 10.3 W m^{-2} τ^{-1}. Our results illustrate that the primary role of dust aerosol is to alter the distribution of solar radiation within the climate system rather than to reflect solar energy to space. We assess the satellite aerosol optical depth products from Mutiangle Imaging Spectroradiometer (MISR) and Moderate Resolution Imaging Spectroradiometer (MODIS) observations by comparing them with our ground-based retrievals. Reasonable agreements with the ground-based observations are found for the MISR product and MODIS Deep Blue product.

Citation: Ge, J. M., J. Su, T. P. Ackerman, Q. Fu, J. P. Huang, and J. S. Shi (2010), Dust aerosol optical properties retrieval and radiative forcing over northwestern China during the 2008 China-U.S. joint field experiment, *J. Geophys. Res.*, *115*, D00K12, doi:10.1029/2009JD013263.

1. Introduction

[2] Atmospheric aerosol is an important factor in climate forcing due to its effect on the solar and terrestrial radiation budget. However, aerosol particles have highly variable optical properties that lead to significant uncertainties in regional and global radiative forcing in terms of its magnitude and even its sign [*Haywood and Boucher*, 2000]. Dust, a major component of aerosol mass loading in many regions, has attracted great scientific interest. In 2006, the U.S. Department of Energy Atmospheric Radiation Measurement (DOE/ARM) Program's Mobile Facility (AMF) was deployed to Africa during the RADAGAST (Radiative Divergence using AMF, GERB and AMMA Stations) experiment [*Miller and Slingo*, 2007] to measure, in part, Sahara dust aerosol optical properties and broadband radiation at both the surface and top of atmosphere (TOA). This experiment provided an opportunity to accurately investigate Sahara dust optical properties and their effects on the radiation budget [*Slingo et al.*, 2006; *McFarlane et al.*, 2009]. In northwest China, the Gobi desert and loess are

[1]Key Laboratory for Semi-Arid Climate Change of the Ministry of Education, College of Atmospheric Sciences, Lanzhou University, Lanzhou, China.
[2]Department of Atmospheric Sciences, University of Washington, Seattle, Washington, USA.

0148-0227/10/2009JD013263

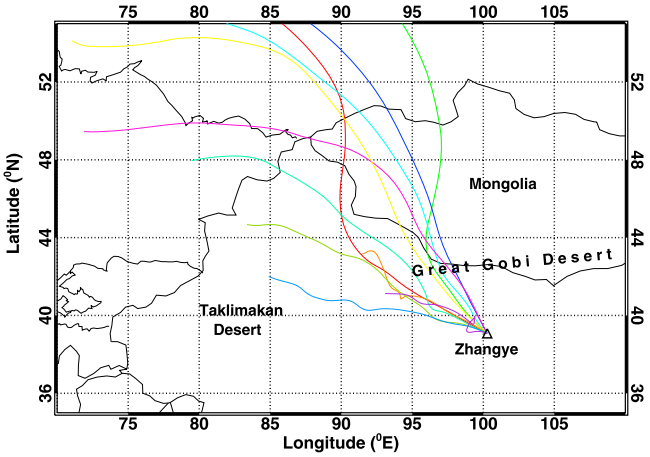

Figure 1. Geographic location of the Zhangye observational site and 72 h HYSPLIT back trajectories analysis at 3 km altitude for the 11 selected cases.

wide spread and are one of the major source regions of Asian dust. In the late winter and early spring of each year, strong winds, which are caused by cold air outbreaks, lift surface material into the free troposphere and transport the dust particles to downwind regions from the Asian continent to west Pacific [*Haywood et al.*, 1999; *Higurashi and Nakajima*, 2002]. These dust particles may have a different physical and chemical composition from those found in other desert areas, such as the Sahara, which results in different optical and radiative properties. In 2008, the largest AMF experiment took place in China with multiple sets of instruments deployed in four locations across China (Z. Li. et al., Overview of the East Asian Study of Tropospheric Aerosols and Impact on Regional Climate (EAST-AIRC), manuscript in preparation, 2010), following a pilot field campaign conducted in China starting in 2005 [*Li et al.*, 2007a]. In order to help characterize dust optical and radiative properties and transport over northwest China, the ARM Ancillary Facility (AAF/SMART-COMMIT, http://smart-commit.gsfc.nasa.gov/) was deployed to a location in the semidesert environment of Zhangye (see Figure 1 for location) for a period of two months from late April to mid June in 2008 (Asian Monsoon Year, AMY-2008, http://www.arm.gov/sites/amf/shouxian/).

[3] Our goal here is to describe the optical properties of the dust aerosol and its impact on the solar radiation budget during the field experiment. First, we use the Multifilter Rotating Shadowband Radiometer (MFRSR) [*Harrison et al.*, 1994] to derive dust aerosol optical depth (AOD) values at the five MFRSR channels. Then, we retrieve the dust aerosol size distribution, single-scattering albedo (SSA) and asymmetry parameter (ASY). A radiative closure experiment is performed to validate the retrieved aerosol optical properties. The Santa Barbara DISORT Atmospheric Radiative Transfer (SBDART, version 2.4 [*Ricchiazzi et al.*, 1998]) model is used to calculate the aerosol effects on the solar energy budget at the surface and TOA. Finally, we compare our retrieved AOD with satellite AOD products including the MODIS standard product [*Kaufman et al.*, 1997a], MODIS Deep Blue product [*Hsu et al.*, 2004], and MISR product [*Diner et al.*, 1998; *Bothwell et al.*, 2002] over this region.

2. Experiment and Data

[4] In 2008, the DOE/ARM Mobile Facility was deployed in China to acquire essential cloud, aerosol, radiative, and meteorological measurements for the study of aerosol indirect effects. The primary site was located at Shouxian in southeast China, which is strongly affected by the Asian monsoon and, therefore, quite moist. Simultaneously, the ARM ancillary facility (AAF) with a subset of AMF instruments, the so-called SMART-COMMIT (Surface-sensing Measurements for Atmospheric Radiative Transfer and Chemical, Optical and Microphysical Measurements of In situ Troposphere), was established at Zhangye to examine dust aerosol specifically. Zhangye (39.082°N, 100.276°E, 1461 m elevation) is at the south edge of Gobi desert and in the semiarid area of northwest China (Figure 1). Each year, dust storms which originate from the Gobi or Taklimakan Desert transport large amounts of dust aerosol over this area [*Huang et al.*, 2007, 2009]. The colored lines in Figure 1 are 72 h back trajectories from the HYSPLIT model (R. R. Draxler and G. D. Rolph, HYSPLIT (Hybrid Single-Particle Lagrangian Integrated Trajectory) model, 2003, http://www.arl.noaa.gov/ready/hysplit4.html) for 11 selected cases that we studied in detail. The back trajectories indicate that these air masses passed through desert regions, where dust aerosols are lifted and transported downwind. There are two major transit paths, one a westerly path through the Taklimakan Desert, and the other a northwesterly path through the Gobi Desert. Strong winds can also lift local dust into the atmosphere near Zhangye.

[5] The AAF/SMART-COMMIT includes a suite of active and passive instruments for measuring meteorological conditions, surface radiative flux and aerosol vertical structure [*Jeong et al.*, 2008]. Beside the AAF data, reflected solar broadband flux data at the TOA from CERES and AOD data from MODIS including both standard and Deep Blue retrievals and MISR are used in our study.

3. Aerosol Single-Scattering Properties Retrieval

[6] There are two available instruments that can be used to retrieve aerosol optical properties at the Zhangye site. One is the Sun and sky radiometer (CIMEL) [*Holben et al.*, 1998] and the other is the MFRSR. CIMEL observe the direct Sun irradiance at eight wavelengths (0.34, 0.38, 0.44, 0.50, 0.67, 0.87, 0.94 and 1.02 μm) and the angular distribution of sky radiances at four wavelengths (0.44, 0.67, 0.87 and 1.02 μm). The wavelength-dependent direct solar radiances are used to calculate AOD while the aureole and sky radiances at larger scattering angles are used to retrieve aerosol size distribution, phase function, and single-scattering albedo values [*Dubovik et al.*, 2000; *Dubovik and King*, 2000]. The MFRSR measures values of the total and diffuse irradiance in 10 nm wide bands peaking at six wavelengths (0.415, 0.500, 0.615, 0.673, 0.870 and 0.940 μm). One of the MFRSR's advantages is that it measures diffuse irradiance from the global sky rather than at some specific scattering angles, therefore, the diffuse signals are much less sensitive to the scattering phase function which is related to particle shape.

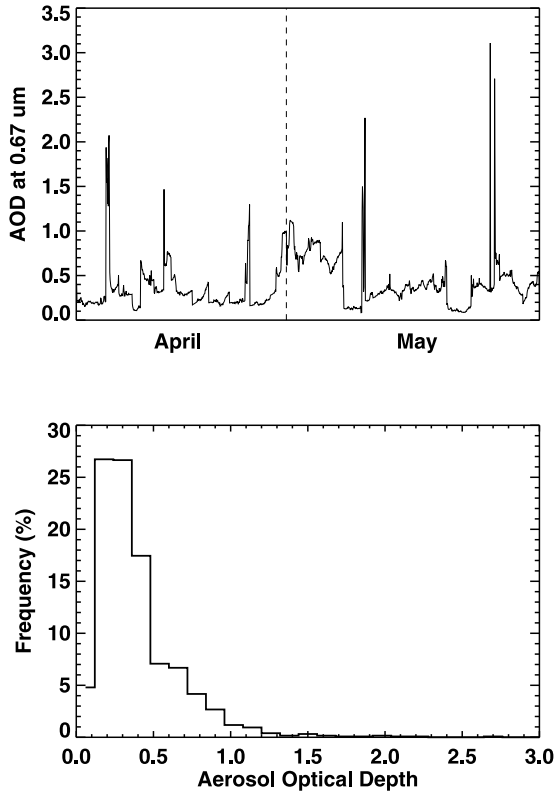

Figure 2. Time series of (top) AOD at 0.67 μm and (bottom) AOD frequency distribution during the periods of April and May from CIMEL measurements.

In our study, we mainly focus on using the MFRSR to retrieve aerosol optical properties.

3.1. Aerosol Optical Depth Retrievals

[7] The MFRSR direct normal irradiances, which are used to derive spectral AOD through the application of Beer's law, are obtained by differencing the total and diffuse irradiances and dividing by the cosine of solar zenith angle.

[8] The linear form of Beer's Law is expressed as

$$\ln I_\lambda = -\tau_\lambda m + \ln I_\lambda^0, \tag{1}$$

where I_λ is the direct normal irradiance reaching the surface at wavelength λ, I_λ^0 is the direct normal irradiance at the TOA, m is the air mass, τ_λ is the total vertical extinction optical thickness of the atmosphere. To obtain τ_λ, we first need to determine I_λ^0, which we do by extrapolation using a Langley regression algorithm [*Harrison and Michalsky*, 1994]. In general, only the most clear days with stable aerosol concentrations can be used to determine I_λ^0, but this rigid requirement is relaxed with the new calibration method proposed by *Lee et al.* [2010]. Once I_λ^0 is well determined, we can easily derive τ_λ from (1). The total optical depth derived from equation (1) has contributions from aerosol (τ_A), Rayleigh scattering (τ_R), ozone absorption (τ_{O3}) and water vapor absorption (τ_{H_2O}) and may be written explicitly as

$$\tau = \tau_A + \tau_R + \tau_{O3} + \tau_{H_2O}. \tag{2}$$

To obtain the aerosol fraction of τ_λ, it is necessary to remove the other contributions. We should mention that NO_2 gas has absorbing effects on the 0.415 and 0.500 μm in heavy urban/industrial pollution area. However, this may be neglected in the rural regions such as the Zhangye site environment.

[9] The Rayleigh scattering contribution is parameterized by [*Liou*, 2002]

$$\tau_{R(\lambda)} = (a + bH)\lambda^{-(c+d\lambda+e/\lambda)}\frac{P}{P_s}, \tag{3}$$

where $a = 0.00864$, $b = 6.5 \times 10^{-6}$, $c = 3.916$, $d = 0.074$, and $e = 0.050$. H and P are the elevation (km) and pressure of the instrument location, respectively. P_s is the sea level pressure. The pressure P is measured by an AAF WXT510 Meteorological Sensor. Ozone optical depths are calculated by multiplying the column ozone particle number by the ozone absorption cross section for each wavelength. Column ozone amounts were obtained from the Total Ozone Mapping Satellite (TOMS) [*Bhartia et al.*, 1993] for each day. Water vapor is transparent for all MFRSR channels except the 0.94 μm channel. It is the dominant absorber at 0.94 μm. Because of this complication, we do not derive AOD for the 0.94 μm channel.

[10] We first give an overall picture of AOD distributions at a wavelength of 0.67 μm as observed from the CIMEL (Figure 2), the standard AERONET (Aerosol Robotic Network) instrument [*Holben et al.*, 1998; *Dubovik et al.*, 2000], during the experiment period of April and May. Figure 2 (top) is the AOD time series. The values of AOD in Zhangye exhibit large variations ranging from a low value of 0.08 to a high of 3.10, which may be caused by a severe dust storm outbreak. Figure 2 (bottom) shows the frequency distribution of AOD at 0.67 μm. Most of the AOD values (75%) are in the range from 0.08 to 0.48. Since we are primarily interested in typical aerosol forcing, we focused on cases with AOD values less than 1. In heavy dust events (AOD > 1), dust particles generally have short lifetimes and relatively brief (but temporarily large) effects on climate radiative forcing.

[11] We identified eleven cases (listed in Table 1), which are mostly or partly clear days, with the AOD values at 0.67 μm ranging from 0.08 to 0.30. As an example, the time series of AOD derived from MFRSR data on 24 April are plotted in Figure 3. The AOD increased slightly in the early morning, reaching a peak at about 0900 (local meridional time, LMT) and then decreased until about 1300 LMT. The AOD values increased sharply in the late afternoon. This phenomenon was also observed in another two cases. One possible cause is that local boundary turbulence lifted dust causing the aerosol loading to increase. The daytime average AOD at 0.67 μm for each case is listed in Table 1. An Angstrom exponent is derived by a linear fit of $\ln(\tau_\lambda)$ against $\ln(\lambda)$ using five wavelengths which can be used as a qualitative indicator of aerosol particle size (also listed in Table 1). The AOD values range from 0.07 on 23 May to 0.29 on 19 May with the standard deviation changing from 0.01 to 0.03.

3.2. Comparison With CIMEL, MISR, MODIS Deep Blue, and Standard Optical Depth

[12] The CIMEL radiometer is the standard AERONET instrument and recognized as a highly accurate Sun pho-

Table 1. MFRSR, CIMEL, Deep Blue, Terra MODIS, and Aqua MODIS Average, Standard Deviation of Aerosol Optical Depths at 0.67 μm Wavelength, and the Angstrom Exponents for Each Case[a]

	AOD (Standard Deviation)					Angstrom Exponent				
Case	MFR	CIM	DB	Terra	Aqua	MFR	CIM	DB	Terra	Aqua
22 April	0.27 (0.04)	0.29 (0.05)	0.15 (0.15)	0.70 (0.11)	0.85 (0.14)	0.34	0.37	0.59	0.50	0.46
23 April	0.20 (0.02)	0.22 (0.04)	0.13 (0.11)	0.47 (0.04)	0.46 (0.08)	0.40	0.33	1.44	1.25	1.26
24 April	0.17 (0.02)	0.18 (0.02)	0.06 (0.01)	0.58 (0.23)	0.46 (0.17)	0.41	0.42	0.97	0.67	0.54
25 April	0.16 (0.01)	0.18 (0.01)	0.30 (0.31)	0.33 (0.07)	0.31 (0.13)	0.41	0.41	0.22	0.81	1.13
27 April	0.15 (0.01)	0.16 (0.02)	0.18 (0.14)	0.32 (0.10)	0.50 (0.26)	0.46	0.43	0.18	0.69	0.53
9 May	0.12 (0.01)	0.10 (0.01)				0.80	0.71			
15 May	0.26 (0.05)	0.25 (0.03)	0.19 (0.18)	0.61 (0.07)	0.77 (0.07)	0.65	0.55	0.31	0.49	0.52
16 May	0.25 (0.04)	0.25 (0.03)	0.23 (0.11)	0.52 (0.01)	0.45 (0.00)	0.69	0.52	1.59	0.88	1.25
19 May	0.29 (0.03)	0.30 (0.03)	0.28 (0.07)	0.57 (0.20)	0.53 (0.12)	0.93	0.85	1.49	0.52	0.53
23 May	0.07 (0.01)	0.08 (0.01)	0.07 (0.04)	0.26 (0.13)	0.17 (0.04)	0.53	0.53	0.97	1.04	0.60
25 May	0.18 (0.01)	0.32 (0.03)	0.17 (0.10)	0.54 (0.10)	0.50 (0.03)	0.70	0.52	1.34	0.60	0.60

[a]Abbreviations: MFR, MFRSR; CIM, CIMEL; DB, Deep Blue; Terra, Terra MODIS; and Aqua, Aqua MODIS.

tometer [*Holben et al.*, 1998; *Dubovik et al.*, 2000]. Thus, we compare our retrieved AOD values from the MFRSR with those from the CIMEL which were processed by AERONET group; however, so far the data is not released on AERONET website. We noticed that people usually use the 0.50 μm channel for comparison. Here, only compare AOD values at 0.67 μm because we not only compare CIMEL with MFRSR, but also do a surface AOD comparison with satellite observations. However, satellites retrieve AOD at 0.55 μm channel instead of 0.50 μm. The 0.67 μm is common channel for both ground and space observations. The MFRSR and CIMEL AOD differences range between 0.00 and 0.02 (Table 1), which is within the limits of calibration accuracy [*Holben et al.*, 1998; *Alexandrov et al.*, 2008], except for the 25 May case where the difference is 0.13. This difference is excessive large, but there is no apparent reason for the disparity. Angstrom exponents derived from the MFRSR and CIMEL wavelength-dependent optical depths are also shown in Table 1. The values of the Angstrom exponents in April are smaller than those in May, indicating that dust particles sizes in April are larger than those in May. The mean particle effective radius R_e of five cases in April is 1.03 ± 0.17 μm, and the mean R_e of the other six cases in May is 0.65 ± 0.09 μm.

[13] Satellite observations are an effective way to provide a global coverage of aerosol optical depth. However, satellite aerosol retrievals are complicated by the fact that the upward radiance received by the satellite is composed of light scattered by the surface and atmospheric constituents, both molecules and particles. Accurate determination of AOD requires the separation of radiation reflected by the surface from that reflected by aerosol. This procedure is difficult over land because land surface reflectances are often large and vary with location and time. Here, we compare our retrieved MFRSR AOD values with MODIS-Terra/Aqua, Deep Blue-Aqua and MISR AOD products to assess the accuracy of satellite AOD values obtained over this semidesert region. Satellite instruments retrieve AOD values from 0.66 μm channel data, which is close to the 0.67 μm channel of the surface instruments. Since dust particles generally have small angstrom exponents, we directly compare satellite AOD_{660} values with ground-based AOD_{670} values, rather than extrapolating them to a common wavelength using an Angstrom parameter. To generate satellite data for comparison with the MFRSR, we consider all available observations within a box of ±0.25° in latitude and longitude centered on the Zhangye site. These AOD values at 0.66 μm, as well as the Angstrom exponent from satellite data, are given in Table 1. We define the absolute relative error for the satellite measurements as $\frac{|AOD_{sat} - AOD_{MFR}|}{AOD_{MFR}}$. 100%. The mean AOD_{670} absolute relative errors between MFRSR and Terra-MODIS, Aqua-MODIS, and Deep Blue are 154.49%, 150.35% and 30.62%, respectively. MISR has a limited swath coverage (360 km) that is much narrow than MODIS (2330 km). At midlatitudes MISR will generally observe a given ground site 3 to 5 times in each 16 day orbital cycle, so, unfortunately, only 2 days of MISR AOD values are available. AOD values for the two cases for which MISR data are available (24 April and 19 May) are plotted in Figure 4. On 19 May (Figure 4, bottom), the aerosol loading is higher with MFRSR AOD values at 0.67 μm of nearly 0.3. Both Deep Blue and MISR AOD retrievals agree well with MFRSR values. Relative errors are within 15% for all wavelengths. On 24 April, aerosol loading is only about half of the 19 May values. The MISR AOD values are still quite similar to the MFRSR values. The maximum absolute relative error between MISR and MFRSR is 45% at 0.446 μm wavelength and the minimum

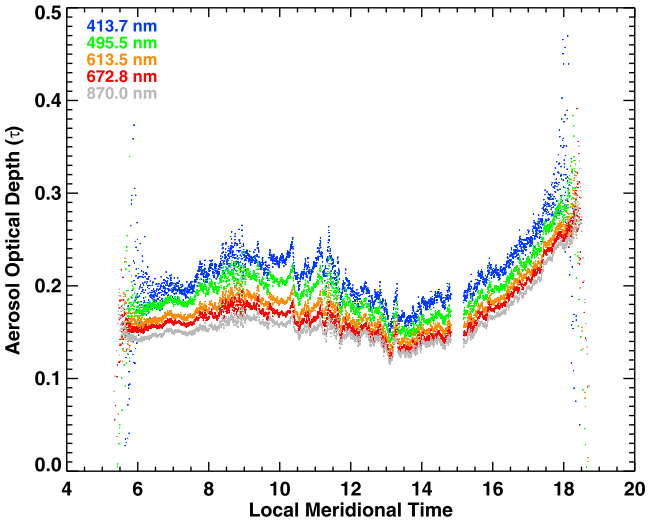

Figure 3. Time series of AOD retrieved from the MFRSR at five wavelengths for the 24 April case.

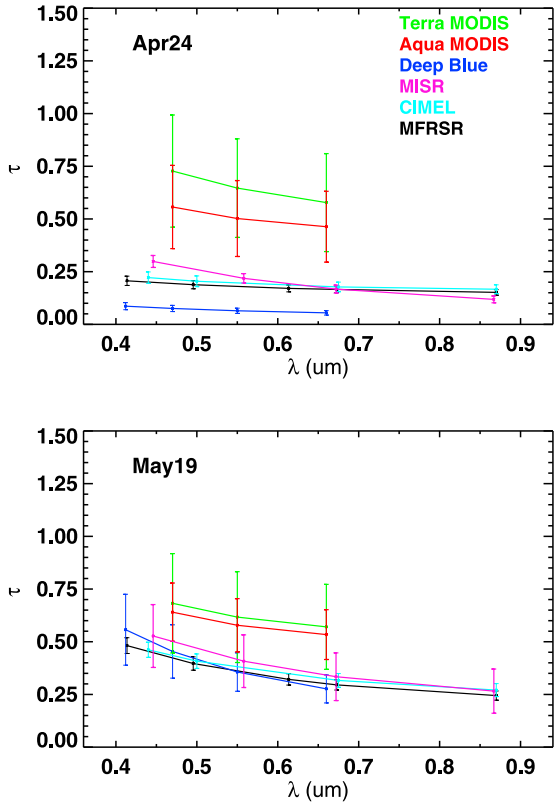

Figure 4. Comparison of Terra MODIS, Aqua MODIS, Deep Blue, MISR, CIMEL and MFRSR aerosol optical depths for (top) 24 April and (bottom) 19 May.

is 0.6% at 0.66 μm. However, the Deep Blue AOD values are much smaller than the MFRSR values in this case with absolute relative errors greater than 70%. MODIS AOD values are much larger than the MFRSR values in both cases.

[14] Although we have only a small data sample, our results suggest strongly that MODIS retrieved AOD values are not reliable over semiarid and arid scenes, most likely because the MODIS operational aerosol retrievals over land use the dark-target approach [*Kaufman et al.*, 1997a]. These errors may be due to two possible reasons. One is that the MODIS retrieval method uses near-infrared (2.1 and 3.8 μm) channels, which in most cases are unaffected by aerosol, to estimate the spectral surface reflectance in each pixel in order to separate the surface and atmospheric components of the radiance received by the satellite. Dust aerosol particles are not transparent at the near-IR wavelengths [*Kaufman et al.*, 1997b] which will induce an underestimation of the surface reflectance and result in an overestimation of AOD. A second reason is that the empirical relationship that is used to deduce surface reflectances of wavelengths of 0.47 and 0.66 μm using the remote sensed surface reflectance values at 2.1 μm [*Kaufman et al.*, 1997b] may be incorrect for bright, semiarid surfaces. The Deep Blue algorithm values are much improved over the MODIS values because Deep Blue employs two blue channels (0.412 and 0.470 μm) in MODIS, for which surface reflectances are relatively small, to infer aerosol properties [*Hsu et al.*, 2004]. The results in Figure 4 show that when the aerosol loading is small (Figure 4, top) in some cases, there can be a significant error in the retrieval of AOD. This could be caused by the neglect of surface bidirectional reflectance distribution function (BRDF) effects when solar zenith angle values are larger than 40 degree during March and April for the mid-latitude desert and semidesert regions in East Asia [*Hsu et al.*, 2006]. Both of the MISR cases show good AOD agreement with surface observations. MISR provides radiance measurements of the same target at nine different viewing angles. Since MISR can remove the atmospheric path contribution from the surface-leaving radiance by taking advantage of differences in multiangular signatures, MISR is much less sensitive to surface type and can successfully retrieve AOD over bright surfaces [*Martonchik et al.*, 1998, 2002].

3.3. Single-Scattering Albedo and Asymmetry Parameter Retrieval

[15] The shapes of dust particles are very irregular. Nonspherical dust particles have quite different scattering phase functions from those of spheres [*Mishchenko et al.*, 1997; *Yang et al.*, 2007], which is quite important in aerosol retrievals that make use of angularly resolved measurements. The MFRSR, however, measures hemisphere irradiances, which are then used to retrieve aerosol optical properties. Consequently, MFRSR retrievals are much less sensitive to the differences of scattering phase function between spherical and nonspherical particles. A systematic study examining the effect of the single-scattering properties (SSP) of nonspherical particles versus those of spheres [*Fu et al.*, 2009] has shown that the relative error of the irradiances due to the assumption of spherical particles is less than 5%. So, here we assume in our retrievals that the dust aerosols are homogeneous spherical particles.

[16] Assuming that aerosol particles are homogeneous spheres, the wavelength-dependent bulk single-scattering albedo (ϖ_λ) and asymmetry parameter (g_λ) may be written as follows:

$$\varpi_\lambda = \frac{\int_{r\min}^{r\max} \pi \cdot r^2 \cdot Q_s(m_\lambda, r/\lambda) \cdot N(r) \cdot dr}{\int_{r\min}^{r\max} \pi \cdot r^2 \cdot Q_e(m_\lambda, r/\lambda) \cdot N(r) \cdot dr}, \tag{4}$$

$$g_\lambda = \frac{\int_{r\min}^{r\max} \pi \cdot r^2 \cdot g(r) \cdot Q_s(m_\lambda, r/\lambda) \cdot N(r) \cdot dr}{\int_{r\min}^{r\max} \pi \cdot r^2 \cdot Q_s(m_\lambda, r/\lambda) \cdot N(r) \cdot dr}, \tag{5}$$

where r is particle radius, $Q_s(m_\lambda, r/\lambda)$ is the scattering efficiency, $Q_e(m_\lambda, r/\lambda)$ is the extinction efficiency, m_λ is refractive index, $N(r)$ is columnar particle number size distribution which is related to the aerosol volume mode by $N(r) \cdot r \cdot (4/3 \cdot \pi \cdot r^3) = dV(r)/d\ln(r)$ [*Kassianov et al.*, 2007]. Here $g(r)$ is the individual particle asymmetry factor. We can simultaneously calculate ϖ_λ and g_λ from Mie theory if $N(r)$ and m_λ are known. Here we follow the method proposed by *Kassianov et al.* [2007] to derive $N(r)$ and estimate the imaginary part of refractive index. The technique comprises two main steps.

[17] The first step provides the aerosol size distribution. The aerosol column-averaged size distribution may be

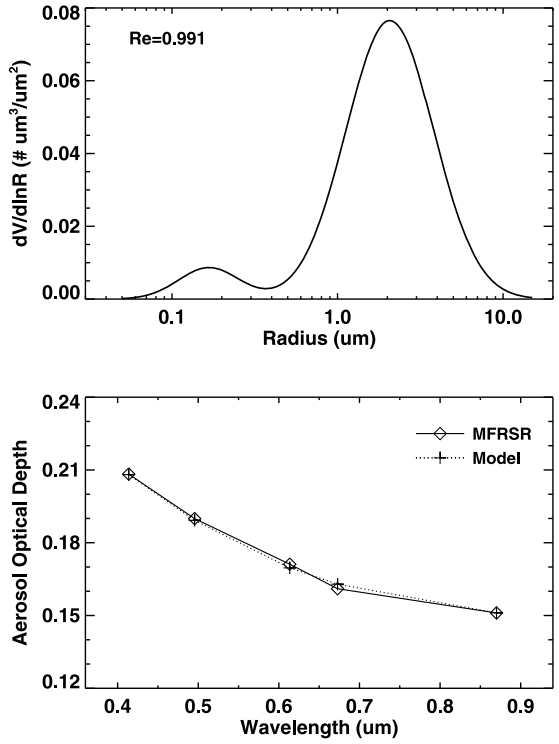

Figure 5. (top) Aerosol size distribution and (bottom) the spectrally dependent AOD values derived from the MFRSR (diamonds) and Mie calculations (crosses) for the 24 April case.

described by a bimodal lognormal distribution that represents the fine mode and coarse mode aerosol [*Dubovik et al.*, 2002],

$$\frac{dV(r)}{d\ln r} = \frac{C_f}{\sqrt{2\pi}\sigma_f}\cdot\exp\left(-\frac{(\ln r-\ln R_f)^2}{2\sigma_f^2}\right)+\frac{C_c}{\sqrt{2\pi}\sigma_c}\cdot\exp\left(-\frac{(\ln r-\ln R_c)^2}{2\sigma_c^2}\right), \quad (6)$$

where C is the particle volume concentration, R is the median radius, σ is the variance and the subscripts f and c stand for fine and coarse modes, respectively. The value of the real part of Asian dust aerosol refractive index reportedly varies from 1.34 to 1.7 [*Kim et al.*, 2005; *Zheng et al.*, 2008]. Here we assume that the real part of the refractive index is 1.5 for each of the MFRSR channel wavelengths and σ is 0.42 for the fine mode and 0.61 for the coarse mode [*Dubovik et al.*, 2002]. We then iterate the other four parameters, C_f, C_c, R_f, R_c, in equation (6) until the RMS difference among the five τ_λ calculated from equation (7), i.e.,

$$\tau_\lambda = \int_{r\min}^{r\max} \pi\cdot r^2\cdot Q_e(m,r/\lambda)\cdot N(r)\cdot dr, \quad (7)$$

and the AOD values derived from MFRSR is a minimum. The imaginary part of the refractive indices is not considered in this step, because the calculation of τ_λ is not sensitive to that value [*King et al.*, 1978]. For this calculation, the initial imaginary part of the refractive index is set to 0.007 for each wavelength. As an example, the result of this process for the 24 April case is shown in Figure 5. The measured and retrieved values of the optical depth are in excellent agreement; the greatest difference is only 1.1% at 0.67 μm wavelength (Figure 5, bottom). The retrieved size distribution is shown in Figure 5 (top). Table 2 lists the retrieved parameters for all cases. The mean values of the fine and coarse modes radii are 0.14 ± 0.03 and 2.22 ± 0.18 μm, respectively, while the mean values of C_f and C_c (which are related to the total volume or mass of each mode) are 0.015 and 0.139, respectively. These results indicate that the particle sizes of the two modes are very consistent during this period and the coarse mode dominates the aerosol volume by about 10:1. This is consistent with our expectation that the majority of the aerosol particles are wind-blown dust.

[18] The second step in the retrieval process is to estimate the imaginary part of the index of refraction using the diffuse-to-direct ratio (DDR) [*Kassianov et al.*, 2007]. We begin by assuming a value of m_λ, which is now the only unknown parameter in equations (4) and (5), from which we can calculate ϖ_λ and g_λ, simultaneously. We then use these aerosol optical properties (ϖ_λ, g_λ and τ_λ) and the Angstrom exponent in a radiative transfer model to obtain a model value of the DDR. We iterate the value of m_λ for each MFRSR wavelength until the differences between the model and observed DDR values are less than 5% for each wavelength. Figure 6 shows the retrieved imaginary refractive index, SSA and asymmetry parameter values as a function of wavelength for the 24 April case. The imaginary part decreases from 0.02 to 0.008 as the wavelength increases from 0.415 to 0.870 μm. The SSA value increases from 0.75 at 0.415 μm to 0.87 at 0.870 μm, while the asymmetry parameter decreases with wavelength from 0.78 to 0.71. The wavelength-dependent SSA and asymmetry parameter values of all cases are given in Table 3. The mean ASY value ranges from 0.74 to 0.70. The mean SSA value increases with wavelength from 0.76 to 0.86. This spectral behavior of dust SSA, indicating decreasing absorption with increasing wavelength, is different from that of urban/industrial and biomass aerosols. This feature was also confirmed by *Dubovik et al.* [2002], *Höller et al.* [2003] and *Bergstrom et al.* [2002], who proposed the idea of using the spectral dependency of SSA to distinguish dust from other aerosol types. Our SSA values are comparable to a recent

Table 2. Parameters of Size Distribution for 11 Cases

Case	C_f (μm^3/μm^2)	R_f (μm)	C_c(μm^3/μm^2)	R_c (μm)
22 April	0.010	0.172	0.209	2.26
23 April	0.011	0.185	0.147	2.30
24 April	0.009	0.167	0.117	2.07
25 April	0.009	0.155	0.124	2.14
27 April	0.010	0.127	0.104	1.91
9 May	0.014	0.131	0.070	1.99
15 May	0.027	0.101	0.211	2.29
16 May	0.025	0.110	0.199	2.32
19 May	0.036	0.125	0.190	2.22
23 May	0.007	0.109	0.060	2.31
25 May	0.011	0.128	0.094	2.57
Mean	0.015	0.137	0.139	2.22
Std dev	0.001	0.028	0.056	0.18

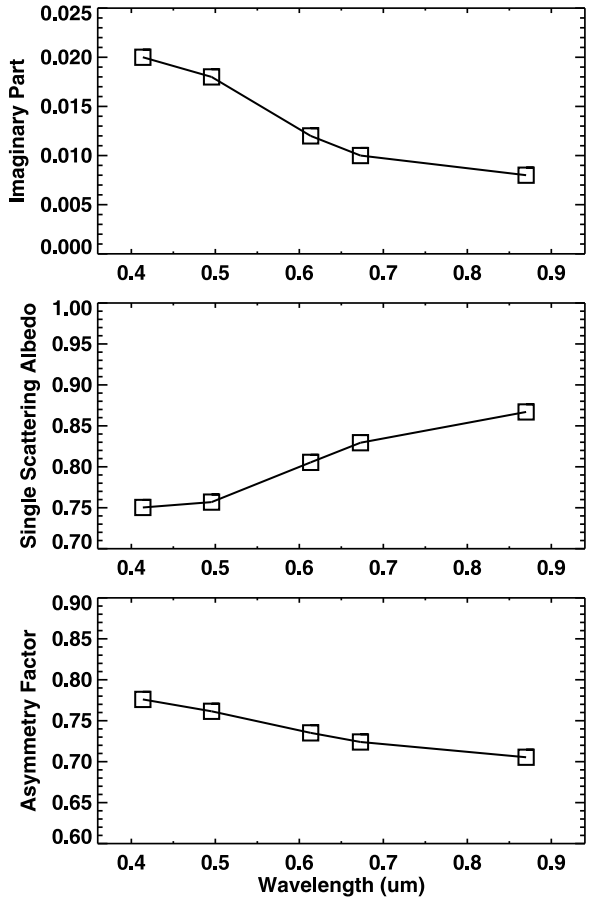

Figure 6. Retrieved spectrally dependent values of the (top) imaginary part of refractive indices, (middle) single-scattering albedo, and (bottom) asymmetry parameter for the 24 April case.

dust optical and radiative forcing study over India [*Pandithurai et al.*, 2008], in which the values of SSA range from 0.74 to 0.84 at 0.5 μm, but are much smaller than those from Africa dust. For example, *Fouquart et al.* [1987] reported a mean value of 0.95. *Haywood et al.* [2003] found that the values of SSA at 0.55 μm ranged from 0.95 to 0.99 during the Saharan Dust Experiment (SHADE). *McFarlane et al.* [2009] derived a mean value of 0.94 at 0.5 μm during the January–April period of 2006. However, our retrieved SSA values are also smaller than some previous results that were obtained from East Asian dust events. *Kim et al.* [2004, 2005] derived the SSA value around 0.89 at 0.5 μm using AERONET data from the Dunhuang site which is 500 km away to the northwest of the Zhangye site. In their work, a lower SSA value of 0.8 was found in the downwind ocean area. They claimed that the reason for the low SSA is because of the mixture of dust aerosols with absorbing anthropogenic aerosols during transport over the industrial and urban areas. *Lee et al.* [2007] derived SSA values by comparing MODIS observed aerosol reflected radiances at the TOA with those calculated from a radiative transfer model. Their SSA values of dust are 0.89 ± 0.04 at 0.5 μm which is similar to Kim's results.

3.4. Radiative Closure Experiment

[19] Given the derived aerosol properties, we can now perform a radiative closure experiment by comparing simulated broadband radiative fluxes (total, direct normal and diffuse) with observations taken on these same days. The most important input variables for the radiative transfer model are the wavelength-dependent column aerosol properties. Other required parameters are the ozone concentration, column water vapor and surface albedo. Good agreement between the calculated and observed radiative fluxes demonstrates that these input parameters, particularly the retrieved aerosol properties, are an appropriate representation of atmospheric conditions. Water vapor and temperature profiles for the calculations are taken from the daily NCEP/NCAR reanalysis data. Ozone concentrations are taken from TOMS and the broadband surface albedo is based on CERES data. To determine the spectrally dependent albedo, we assume that the surface was composed of sand and vegetation and then adjust the mixing fraction of sand and vegetation until the broadband surface albedo derived from the spectral shape matches the CERES observation. For all cases, the averaged broadband surface albedo used in the model is 0.21. The fractions of sand and vegetation are 85% and 15%, respectively.

[20] The observed instantaneous solar broadband (0.3–3 μm) total, diffuse, and direct normal fluxes are compared with model-simulated fluxes for the 24 April case in Figure 7.

Table 3. Wavelength-Dependent SSA and ASY for 11 Cases

	Single-Scattering Albedo					Asymmetry Parameter				
Case	0.415 μm Wavelength	0.500 μm Wavelength	0.615 μm Wavelength	0.673 μm Wavelength	0.870 μm Wavelength	0.415 μm Wavelength	0.500 μm Wavelength	0.615 μm Wavelength	0.673 μm Wavelength	0.870 μm Wavelength
22 April	0.72	0.73	0.78	0.81	0.86	0.80	0.79	0.76	0.75	0.72
23 April	0.75	0.76	0.80	0.82	0.86	0.79	0.77	0.75	0.73	0.71
24 April	0.75	0.76	0.81	0.83	0.87	0.78	0.76	0.74	0.72	0.71
25 April	0.74	0.75	0.80	0.82	0.86	0.78	0.76	0.74	0.73	0.71
27 April	0.75	0.75	0.80	0.83	0.87	0.75	0.74	0.72	0.71	0.70
9 May	0.80	0.79	0.83	0.84	0.87	0.71	0.70	0.68	0.67	0.67
15 May	0.75	0.74	0.78	0.81	0.85	0.71	0.70	0.70	0.70	0.70
16 May	0.76	0.75	0.79	0.81	0.85	0.71	0.71	0.70	0.70	0.70
19 May	0.80	0.79	0.82	0.83	0.86	0.71	0.69	0.67	0.67	0.67
23 May	0.75	0.74	0.78	0.81	0.85	0.72	0.72	0.71	0.71	0.71
25 May	0.75	0.74	0.77	0.79	0.84	0.72	0.71	0.71	0.71	0.71
Mean	0.76	0.75	0.80	0.82	0.86	0.74	0.73	0.72	0.71	0.70
Std dev	0.02	0.02	0.02	0.01	0.01	0.04	0.03	0.03	0.02	0.02

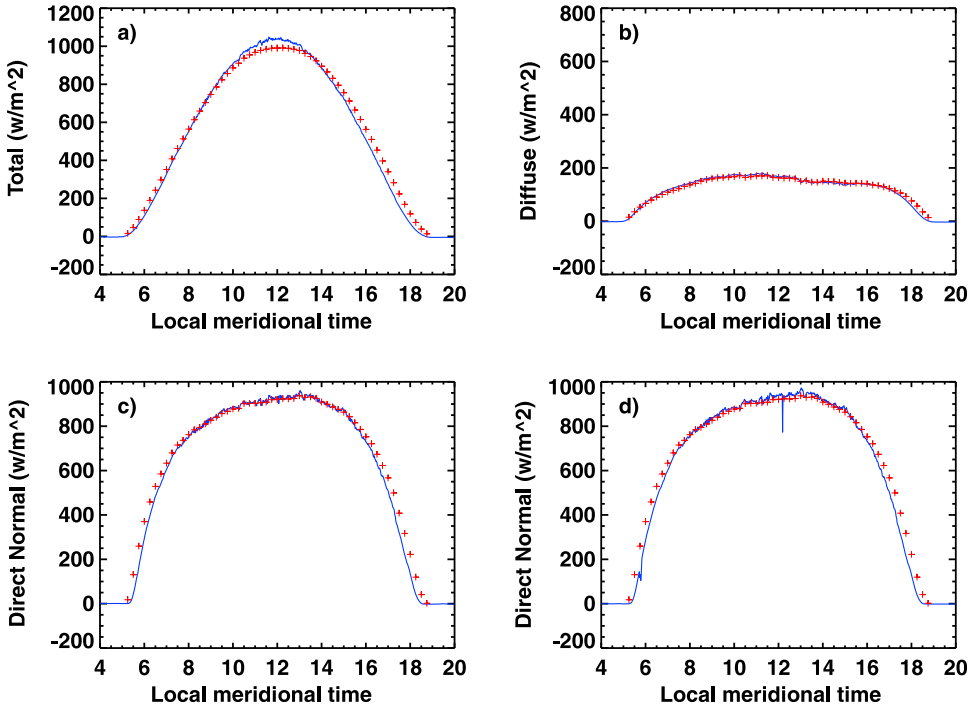

Figure 7. Observed (blue line) and calculated (red crosses) broadband (a) total, (b) diffuse, and (c and d) direct normal solar surface fluxes for the April 24 case. The observational data in Figures 7c and 7d were acquired by two different instruments.

The total flux was measured with a Precision Spectral Pyranometer and the diffuse flux with a CM21 pyranometer. Two independent measurements of the direct normal flux were made with an Eppley Normal Incidence Pyrheliometer and a CH1 NIP. The daylight-averaged differences between simulated and observed total, diffuse and direct normal flux are −3.6, 0.9, 0.8 W m^{-2}, respectively, on 24 April. Note that the aerosol size distribution properties are assumed constant for the day, but the instantaneous values of the aerosol optical depth (Figure 3) are used in these calculations.

[21] The flux closure results for the 6 days that were cloud free are shown in Table 4. The daylight-averaged differences are −8.5 W m^{-2} for the total flux, −2.9 W m^{-2} for the diffuse flux, and −2.1 W m^{-2} for the direct normal flux. We also compared the upwelling fluxes (0.3–5 μm) at the TOA from the model with available CERES measurements (Figure 8) within the box of ±0.25° for six cases which were cloud free when the Aqua satellite passed over the surface site. The mean difference in the instantaneous TOA fluxes between the model and CERES is 8.0 W m^{-2}.

[22] In general, the good agreement of the direct normal fluxes indicates that the AOD thickness and gas absorption values are accurate, both in magnitude and spectral dependence. The good agreement of the diffuse fluxes indicates that the retrieved single-scattering albedos and asymmetry parameters are reasonable. Because these parameter values were selected by matching the narrowband diffuse fluxes at five wavelengths, it is perhaps to be expected that the broadband diffuse fluxes should also be in good agreement. Since the ground-based measured total and diffuse fluxes are insensitive to surface albedo, especially when the surface

Table 4. Observed and Calculated Daylight Mean Solar Flux for Six Noncloudy Days of the 11 Cases

	Total SW Flux (W m^{-2})	Diffuse SW Flux (W m^{-2})	Direct SW Flux (W m^{-2})
Mean observed flux	609.82	136.94	674.66
Mean simulated flux	601.28	134.04	672.59
Mean flux difference (model - observed)	−8.54	−2.90	−2.07

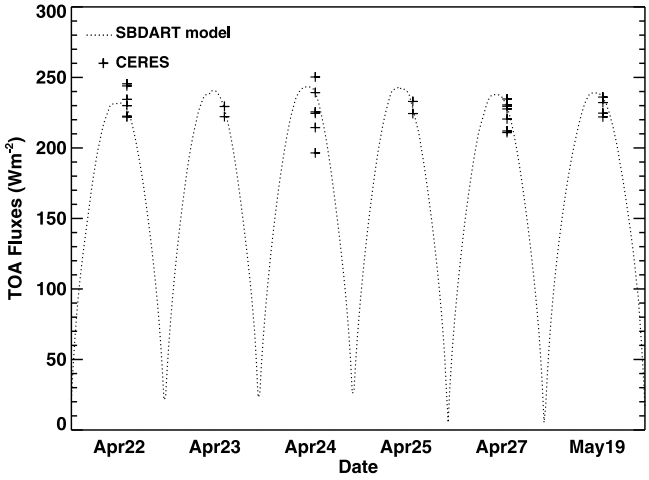

Figure 8. CERES observed (crosses) and model-simulated (dotted lines) upward solar broadband fluxes (0.3–5 μm) at the TOA. The valid CERES values are obtained within a box of ±0.25° in latitude and longitude centered on the Zhangye site.

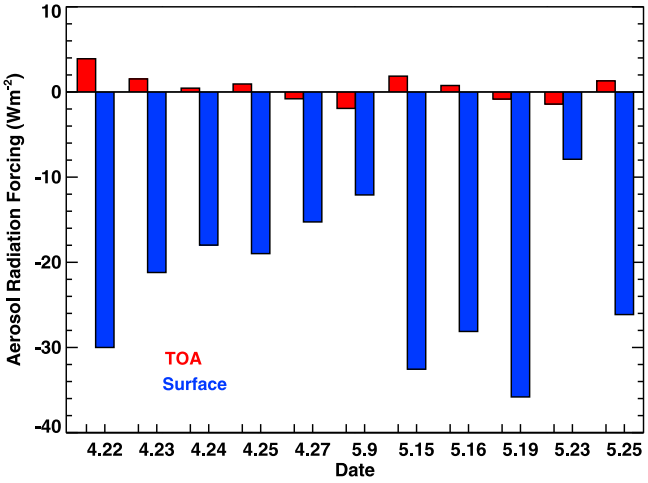

Figure 9. Daily averaged direct aerosol radiative forcing at the surface (blue bars) and TOA (red bars) for the 11 cases. Dates are given as, for example, 4.22 for 22 April.

albedo is small, the consistence of simulated fluxes at the TOA with CERES observations supports that the surface albedo we used in the model is correct.

4. Direct Aerosol Radiative Forcing

[23] Having determined the aerosol parameters that provide a good match between calculated and observed fluxes, we are now in position to determine the direct aerosol forcing due to the dust. Using the aerosol optical depth, SSA, ASY and the other parameters as discussed above and the SBDART model, we calculate instantaneous aerosol radiative forcing (ARF) in 15 min intervals by subtracting the net flux (downward-upward) calculated with aerosol from calculations without aerosol. In order to calculate the daily averaged radiative forcing, we assume that the aerosol concentration remains relatively constant during the day and interpolated AOD across periods when clouds were present in some cases. Figure 9 shows the 24 h averaged ARF values at both surface and TOA for the 11 cases. Dust aerosol has a strong negative forcing at the surface, which could significantly reduce surface temperature, ranging from -7.9 to -35.8 W m^{-2} and a mean value of -22.4 ± 8.9 W m^{-2} per day. The maximum value occurs on 19 May coinciding with the largest AOD. The surface dust ARF estimated in Niamey [*McFarlane et al.*, 2009] is -21.1 ± 14.3 W m^{-2} and the values of ARF estimated at three ground sites over East Asia [*Kim et al.*, 2005] range from -13 to -43 W m^{-2}, which are comparable to our results. However, the dust aerosol in our study has smaller AOD values and stronger absorption (smaller SSA values).

[24] On a global basis, direct aerosol radiative forcing at the TOA is generally determined to be negative [*Yu et al.*, 2006; *Kim and Ramanathan*, 2008], indicating a cooling effect of aerosol on climate system. Our results, on a regional scale, show that the magnitude of dust ARF at the TOA is small (less than 4 W m^{-2}) and the sign can be either positive or negative depending on the SSA value in each case. This implies that dust aerosols over the semidesert area have little effect on the TOA solar radiation budget. Similar results were obtained in many other places in China in the north [*Li et al.*, 2007b], south [*Xia et al.*, 2007] and across China [*Li et al.*, 2010], impliying moderately strong absorbing aerosols. Global aerosol radiative effects on climate are a sum of regional effects, which exhibit significant differences depending on aerosol type and surface albedo.

[25] The large ARF difference between TOA and surface, which represents absorbed solar radiation within the atmosphere, heats the atmosphere, reduces eddy heat convergence, and induces a reduction in surface temperature [*Miller and Tegen*, 1998, 1999]. Heating the atmosphere and cooling the surface can change the boundary layer vertical temperature gradient and may be expected to reduce evaporation and cloud formation [*Hansen et al.*, 1997; *Ackerman et al.*, 2000] and weaken the hydrological cycle [*Ramanathan et al.*, 2001].

[26] We also compute the daily averaged surface aerosol radiative forcing efficiency (ARFE), which is defined as the diurnally averaged ARF divided by the daily averaged AOD. For easy comparison to other work, we used the AOD at 0.5 μm to calculate the ARFE. The average surface ARFE is -95.1 ± 10.3 W m^{-2} τ^{-1}. The absolute value is nearly 40 W m^{-2} τ^{-1} larger than the value estimated in Niamey during the 2006 spring season [*McFarlane et al.*, 2009] because of lower SSA values retrieved here. *Kim et al.* [2005] pointed out that the values of ARFE due to Asian dust range from -55 to -106 W m^{-2} τ^{-1}. Our results are at the larger (in absolute value) end of this range. However, Kim et al. claimed that the large ARFE values are enhanced possibly by mixing with soot particles. The relationship between SSA and surface ARFE for our 11 cases is shown in Figure 10. As expected, lower values of SSA produce greater negative surface ARFE values.

5. Summary

[27] The ARM AAF was deployed to the semidesert area of Zhangye, which is located in Northwest China, in order to monitor dust aerosol optical properties and its radiative effects. In this paper, we assume that the shape of dust particles is spherical and focus on using MFRSR measure-

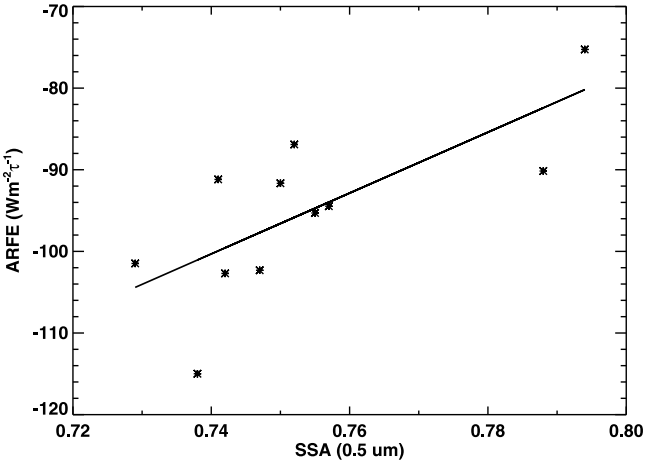

Figure 10. Daily averaged surface aerosol radiative forcing efficiency (ARFE) versus SSA at 0.5 μm wavelength for the 11 cases.

ments to retrieve dust aerosol optical properties and then using these properties to calculate solar dust radiative forcing. The retrieved volume size distributions indicate the dominance of large dust particles. The SSA shows an increasing trend with wavelength, indicating stronger dust aerosol absorption at shorter wavelength. The values of SSA, which range from 0.76 ± 0.02 to 0.86 ± 0.01, are much lower than those derived in Africa and also relatively smaller than former results obtained over East Asia.

[28] Before calculating the dust aerosol radiative forcing, we carried out a radiative closure experiment. All the radiative transfer model input parameters, including AOD, SSA, ASY, Angstrom exponent, water vapor, ozone, surface albedo, are from either ground or satellite measurements. The observed and simulated solar broadband total, direct normal and diffuse fluxes agree well with each other. Especially, the mean difference between calculated and observed diffuse fluxes, which was significant and pointed out as a longstanding problem in previous work [*Kato et al.*, 1997; *Halthore et al.*, 2004], is only -2.9 W m^{-2}. The good agreement between simulations and observations verifies that the retrieved aerosol optical properties and the other input parameters in the SBDART model are appropriate to represent the real atmosphere conditions.

[29] We then estimate the solar dust aerosol radiative forcing at both the surface and TOA. The calculated ARF at the TOA has a small magnitude (less than 4 W m^{-2}). The ARF values at the surface show a consistent cooling effect. The 24 h average surface ARF changes from -7.9 to -35.8 W m^{-2} due to the variability of aerosol loading. The average surface ARFE (at 0.5 μm) is -95.1 ± 10.3 W m^{-2} τ^{-1}. Our ARFE value is considerably larger in absolute value than the value derived in Niamey, which implies that Asian dust produces a greater radiative forcing per unit aerosol loading.

[30] We also compare our retrieved aerosol optical depth with CIMEL and satellite products. Our retrievals agree well with CIMEL AOD in most of the cases except 25 May. The AOD values are overestimated more than 150% by the MODIS standard products over the semidesert region. The MODIS Deep Blue product performs better, the mean relative error between Deep Blue and MFRSR is 30.62% at 0.67 μm. MISR performs the best retrievals as compared with MFRSR. However, we have only 2 days of MISR data due to its limited swath coverage.

[31] Our study is limited by the relatively few days of clear-sky data available from the AAF deployment. Data are currently being acquired by Lanzhou University and we anticipate extending this work in the future analyzing these data. Our results from the 11 days are consistent and highlight the importance of dust aerosol in semiarid regions in increasing solar absorption in the atmosphere at the expense of solar absorption at the surface. The impact of this on surface heating and boundary layer growth is under investigation.

[32] **Acknowledgments.** This research is supported by the National Science Foundation of China under grants 40628005 and 40633017, the Chang-Jiang Visiting Professor fund, and the Fundamental Research Funds for the Central University (lzujbky-2009-157). Q.F. is in part supported by DOE grant DE-FG02-09ER64769 and by NASA grant NNX09AH73G.

References

Ackerman, A. S., O. B. Toon, D. E. Stevens, A. J. Heymsfield, V. Ramanathan, and E. J. Welton (2000), Reduction of tropical cloudiness by soot, *Science*, *288*, 1042–1047, doi:10.1126/science.288.5468.1042.

Alexandrov, M. D., A. A. Lacis, B. E. Carlson, and B. Cairns (2008), Characterization of atmospheric aerosols using MFRSR measurements, *J. Geophys. Res.*, *113*, D08204, doi:10.1029/2007JD009388.

Bergstrom, R. W., P. B. Russell, and P. Hignett (2002), Wavelength dependence of the absorption of black carbon particles: Predictions and results from the TARFOX experiment and implications for the aerosol single scattering albedo, *J. Atmos. Sci.*, *59*, 567–577, doi:10.1175/1520-0469(2002)059<0567:WDOTAO>2.0.CO;2.

Bhartia, P. K., J. Herman, R. D. McPeters, and O. Torres (1993), Effect of Mount Pinatubo aerosols on total ozone measurements from backscatter ultraviolet (BUV) experiments, *J. Geophys. Res.*, *98*, 18,547–18,554, doi:10.1029/93JD01739.

Bothwell, G. W., E. G. Hansen, R. E. Vargo, and K. C. Miller (2002), The Multi-angle Imaging SpectroRadiometer science data system, its products, tools and performance, *IEEE Trans. Geosci. Remote Sens.*, *40*(7), 1467–1476, doi:10.1109/TGRS.2002.801152.

Diner, D. J., et al. (1998), Multi-angle Imaging SpectroRadiometer (MISR) description and experiment overview, *IEEE Trans. Geosci. Remote Sens.*, *36*(4), 1072–1087, doi:10.1109/36.700992.

Dubovik, O., and M. D. King (2000), A flexible inversion algorithm for retrieval of aerosol optical properties from Sun and sky radiance measurements, *J. Geophys. Res.*, *105*, 20,673–20,696, doi:10.1029/2000JD900282.

Dubovik, O., A. Smirnov, B. N. Holben, M. D. King, Y. J. Kaufman, T. F. Eck, and I. Slutsker (2000), Accuracy assessments of aerosol properties retrieved from AERONET Sun and sky radiance measurements, *J. Geophys. Res.*, *105*, 9791–9806, doi:10.1029/2000JD900040.

Dubovik, O., B. N. Holben, T. F. Eck, A. Smirnov, Y. J. Kaufman, M. D. King, D. Tanre, and I. Slutsker (2002), Variability of absorption and optical properties of key aerosol types observed in worldwide locations, *J. Atmos. Sci.*, *59*, 590–608, doi:10.1175/1520-0469(2002)059<0590:VOAAOP>2.0.CO;2.

Fouquart, Y., B. Bonnel, G. Brogniez, J. C. Buriez, L. Smith, J. J. Morcrette, and A. Cerf (1987), Observations of Saharan aerosols: Results of ECLATS field experiment. Part II: Broadband radiative characteristics of the aerosols and vertical radiative flux divergence, *J. Clim. Appl. Meteorol.*, *26*, 38–52, doi:10.1175/1520-0450(1987)026<0038:OOSARO>2.0.CO;2.

Fu, Q., T. J. Thorsen, J. Su, J. M. Ge, and J. P. Huang (2009), Test of Mie-based single-scattering properties of non-spherical dust aerosols in radiative flux calculations, *J. Quant. Spectrosc. Radiat. Transfer*, *110*, 1640–1653, doi:10.1016/j.jqsrt.2009.03.010.

Halthore, R. N., M. A. Miller, J. A. Ogren, P. J. Sheridan, D. W. Slaterand, and T. Stoffel (2004), Further developments in closure experiments for surface diffuse irradiance under cloud-free skies at a continental site, *Geophys. Res. Lett.*, *31*, L07111, doi:10.1029/2003GL019102.

Hansen, J., M. Sato, and R. Ruedy (1997), Radiative forcing and climate response, *J. Geophys. Res.*, *102*, 6831–6864, doi:10.1029/96JD03436.

Harrison, L., and J. Michalsky (1994), Objective algorithms for the retrieval of optical depths from ground-based measurements, *Appl. Opt.*, *33*(22), 5126–5132, doi:10.1364/AO.33.005126.

Harrison, L., J. Michalsky, and J. Berndt (1994), Automated multifilter rotating shadow-band radiometer: An instrument for optical depth and radiation measurements, *Appl. Opt.*, *33*(22), 5118–5125, doi:10.1364/AO.33.005118.

Haywood, J. M., and O. Boucher (2000), Estimates of the direct and indirect radiative forcing due to tropospheric aerosols: A review, *Rev. Geophys.*, *38*, 513–543, doi:10.1029/1999RG000078.

Haywood, J., V. Ramaswamy, and B. J. Soden (1999), Tropospheric aerosol climate forcing in clear-sky satellite observations over the oceans, *Science*, *283*, 1299–1303, doi:10.1126/science.283.5406.1299.

Haywood, J. M., P. Francis, S. Osborne, M. Glew, N. Loeb, E. Highwood, D. Tanre, G. Myhre, P. Formenti, and E. Hirst (2003), Radiative properties and direct radiative effect of Saharan dust measured by the C-130 aircraft during SHADE: 1. Solar spectrum, *J. Geophys. Res.*, *108*(D18), 8577, doi:10.1029/2002JD002687.

Higurashi, A., and T. Nakajima (2002), Detection of aerosol types over the East China Sea near Japan from four-channel satellite data, *Geophys. Res. Lett.*, *29*(17), 1836, doi:10.1029/2002GL015357.

Holben, B. N., et al. (1998), AERONET-A federated instrument network and data archive for aerosol characterization, *Remote Sens. Environ.*, *66*(1), 1–16, doi:10.1016/S0034-4257(98)00031-5.

Höller, R., K. Ito, S. Tohno, and M. Kasahara (2003), Wavelength-dependent aerosol single-scattering albedo: Measurements and model

calculations for a coastal site near the Sea of Japan during ACE-Asia, *J. Geophys. Res.*, *108*(D23), 8648, doi:10.1029/2002JD003250.

Hsu, N. C., S. C. Tsay, M. D. King, and J. R. Herman (2004), Aerosol properties over bright-reflecting source regions, *IEEE Trans. Geosci. Remote Sens.*, *42*, 557–569, doi:10.1109/TGRS.2004.824067.

Hsu, N. C., S.-C. Tsay, M. D. King, and J. R. Herman (2006), Deep Blue retrievals of Asian aerosol properties during ACE-Asia, *IEEE Trans. Geosci. Remote Sens.*, *44*, 3180–3195, doi:10.1109/TGRS.2006.879540.

Huang, J., P. Minnis, Y. Yi, Q. Tang, X. Wang, Y. Hu, Z. Liu, K. Ayers, C. Trepte, and D. Winker (2007), Summer dust aerosols detected from CALIPSO over the Tibetan Plateau, *Geophys. Res. Lett.*, *34*, L18805, doi:10.1029/2007GL029938.

Huang, J. P., Q. Fu, J. Su, Q. Tang, P. Minnis, Y. Hu, Y. Yi, and Q. Zhao (2009), Taklimakan dust aerosol radiative heating derived from CALIPSO observations using the Fu-Liou radiation model with CERES constraints, *Atmos. Chem. Phys.*, *9*, 4011–4021, doi:10.5194/acp-9-4011-2009.

Jeong, M.-J., S.-C. Tsay, Q. Ji, N. C. Hsu, R. A. Hansell, and J. Lee (2008), Ground-based measurements of airborne Saharan dust in marine environment during the NAMMA field experiment, *Geophys. Res. Lett.*, *35*, L20805, doi:10.1029/2008GL035587.

Kassianov, E. I., C. J. Flynn, T. P. Ackerman, and J. C. Barnard (2007), Aerosol single-scattering albedo and asymmetry parameter from MFRSR observations during the ARM Aerosol IOP 2003, *Atmos. Chem. Phys.*, *7*, 3341–3351, doi:10.5194/acp-7-3341-2007.

Kato, S., T. P. Ackerman, E. E. Clothiaux, J. H. Mather, G. G. Mace, M. L. Wesely, F. Murcray, and J. Michalsky (1997), Uncertainties in modeled and measured clear-sky surface shortwave irradiances, *J. Geophys. Res.*, *102*, 25,881–25,898, doi:10.1029/97JD01841.

Kaufman, Y. J., D. Tanre, L. A. Remer, E. Vermote, A. Chu, and B. N. Holben (1997a), Operational remote sensing of tropospheric aerosol over land from EOS moderate resolution imaging spectroradiometer, *J. Geophys. Res.*, *102*, 17,051–17,067, doi:10.1029/96JD03988.

Kaufman, Y. J., A. E. Wald, L. A. Remer, B.-C. Gao, R.-R. Li, and L. Flynn (1997b), The MODIS 2.1-μm channel-correlation with visible reflectance for use in remote sensing of aerosol, *IEEE Trans. Geosci. Remote Sens.*, *355*, 1286–1298, doi:10.1109/36.628795.

Kim, D.-H., and V. Ramanathan (2008), Solar radiation budget and radiative forcing due to aerosols and clouds, *J. Geophys. Res.*, *113*, D02203, doi:10.1029/2007JD008434.

Kim, D.-H., B. J. Sohn, T. Nakajima, T. Takamura, T. Takemura, B. C. Choi, and S. C. Yoon (2004), Aerosol optical properties over East Asia determined from ground-based sky radiation measurements, *J. Geophys. Res.*, *109*, D02209, doi:10.1029/2003JD003387.

Kim, D.-H., B. J. Sohn, T. Nakajima, and T. Takamura (2005), Aerosol radiative forcing over East Asia determined from ground-based solar radiation measurements, *J. Geophys. Res.*, *110*, D10S22, doi:10.1029/2004JD004678.

King, M. D., D. M. Byrne, B. M. Herman, and J. A. Reagan (1978), Aerosol size distributions obtained by inversion of spectral optical depth measurements, *J. Atmos. Sci.*, *35*, 2153–2167, doi:10.1175/1520-0469(1978)035<2153:ASDOBI>2.0.CO;2.

Lee, K.-H., Z. Li, M.-S. Wong, J. Xin, W.-M. Hao, and F. Zhao (2007), Aerosol single scattering albedo estimated across China from a combination of ground and satellite measurements, *J. Geophys. Res.*, *112*, D22S15, doi:10.1029/2007JD009077.

Lee, K. H., Z. Li, M. C. Cribb, J. Liu, L. Wang, Y. Zheng, X. Xia, H. Chen, and B. Li (2010), Aerosol optical depth measurements in eastern China and a new calibration method, *J. Geophys. Res.*, doi:10.1029/2009JD012812, in press.

Li, Z., K.-H. Lee, Y. Wang, J. Xin, and W. M. Hao (2010), First observation-based estimates of cloud-free aerosol radiative forcing across China, *J. Geophys. Res.*, doi:10.1029/2009JD013306, in press.

Li, Z., et al. (2007a), Preface to special section on East Asian Study of Tropospheric Aerosols: An International Regional Experiment (EAST-AIRE), *J. Geophys. Res.*, *112*, D22S00, doi:10.1029/2007JD008853.

Li, Z., et al. (2007b), Aerosol optical properties and their radiative effects in northern China, *J. Geophys. Res.*, *112*, D22S01, doi:10.1029/2006JD007382.

Liou, K. N. (2002), *An Introduction to Atmospheric Radiation*, Academic, San Diego, Calif.

Martonchik, J. V., D. J. Diner, B. Pinty, M. M. Verstraete, R. B. Myneni, Y. Knyazikhin, and H. R. Gordon (1998), Determination of land and ocean reflective, radiative and biophysical properties using multi-angle imaging, *IEEE Trans. Geosci. Remote Sens.*, *36*, 1266–1281, doi:10.1109/36.701077.

Martonchik, J. V., D. J. Diner, K. A. Crean, and M. A. Bull (2002), Regional aerosol retrieval results from MISR, *IEEE Trans. Geosci. Remote Sens.*, *40*, 1520–1531, doi:10.1109/TGRS.2002.801142.

McFarlane, S. A., E. I. Kassianov, J. Barnard, C. Flynn, and T. P. Ackerman (2009), Surface shortwave aerosol radiative forcing during the Atmospheric Radiation Measurement Mobile Facility deployment in Niamey, Niger, *J. Geophys. Res.*, *114*, D00E06, doi:10.1029/2008JD010491.

Miller, M., and A. Slingo (2007), The Arm Mobile Facility and its first international deployment: Measuring radiative flux divergence in west Africa, *Bull. Am. Meteorol. Soc.*, *88*, 1229–1244, doi:10.1175/BAMS-88-8-1229.

Miller, R. L., and I. Tegen (1998), Climate response to soil dust aerosols, *J. Clim.*, *11*, 3247–3267, doi:10.1175/1520-0442(1998)011<3247:CRTSDA>2.0.CO;2.

Miller, R. L., and I. Tegen (1999), Radiative forcing of a tropical direct circulation by soil dust aerosols, *J. Atmos. Sci.*, *56*, 2403–2433, doi:10.1175/1520-0469(1999)056<2403:RFOATD>2.0.CO;2.

Mishchenko, M. I., L. D. Travis, R. A. Kahn, and R. A. West (1997), Modeling phase functions for dustlike tropospheric aerosols using a shape mixture of randomly oriented polydisperse spheroids, *J. Geophys. Res.*, *102*, 16,831–16,847, doi:10.1029/96JD02110.

Pandithurai, G., S. Dipu, K. K. Dani, S. Tiwari, D. S. Bisht, P. C. S. Devara, and R. T. Pinker (2008), Aerosol radiative forcing during dust events over New Delhi, India, *J. Geophys. Res.*, *113*, D13209, doi:10.1029/2008JD009804.

Ramanathan, V., P. J. Crutzen, J. L. Kiehl, and D. Rosenfeld (2001), Aerosols, climate, and the hydrological cycle, *Science*, *294*, 2119–2124, doi:10.1126/science.1064034.

Ricchiazzi, P., S. Yang, C. Gautier, and D. Sowle (1998), SBDART: A research and teaching software tool for plane-parallel radiative transfer in the Earth's atmosphere, *Bull. Am. Meteorol. Soc.*, *79*, 2101–2114, doi:10.1175/1520-0477(1998)079<2101:SARATS>2.0.CO;2.

Slingo, A., et al. (2006), Observations of the impact of a major Saharan dust storm on the atmospheric radiation balance, *Geophys. Res. Lett.*, *33*, L24817, doi:10.1029/2006GL027869.

Xia, X., Z. Li, B. Holben, P. Wang, T. Eck, H. Chen, M. Cribb, and Y. Zhao (2007), Aerosol optical properties and radiative effects in the Yangtze Delta region of China, *J. Geophys. Res.*, *112*, D22S12, doi:10.1029/2007JD008859.

Yang, P., Q. Feng, G. Hong, G. W. Kattawar, W. J. Wiscombe, M. I. Mishchenko, O. Dubovik, I. Laszlo, and I. N. Sokolik (2007), Modeling of the scattering and radiative properties of nonspherical dust like aerosols, *J. Aerosol Sci.*, *38*, 995–1014, doi:10.1016/j.jaerosci.2007.07.001.

Yu, H., et al. (2006), A review of measurement-based assessments of the aerosol direct radiative effect and forcing, *Atmos. Chem. Phys.*, *6*, 613–666, doi:10.5194/acp-6-613-2006.

Zheng, Y., J. Liu, R. Wu, Z. Li, B. Wang, and T. Tamio (2008), Seasonal statistical characteristics of aerosol optical properties at a site near a dust region in China, *J. Geophys. Res.*, *113*, D16205, doi:10.1029/2007JD009384.

T. P. Ackerman, Department of Atmospheric Sciences, University of Washington, Seattle, WA 98105, USA.

Q. Fu, J. M. Ge, J. P. Huang, J. S. Shi, and J. Su, Key Laboratory for Semi-Arid Climate Change of the Ministry of Education, College of Atmospheric Sciences, Lanzhou University, Lanzhou 730000, China. (gejm@lzu.edu.cn)